# Supplementary materials for "Hierarchy of bound states in the one-dimensional ferromagnetic Ising chain $CoNb_2O_6$ investigated by high-resolution time-domain terahertz spectroscopy"

## 1 Terahertz technique

The time domain terahertz spectroscopy setup used in this work is shown in Fig. S1. A KM Labs Ti:Sapph modelocked laser is used to generate ∼60 femtosecond duration NIR pulses centered at 820 nm with an 80 MHz repetition rate. A beam splitter divides each pulse into two different paths. The first part of the pulse is used to excite a photoconductive Auston-switch antenna. This antenna is voltage biased, which causes charge to accelerate across the small antenna gap, emitting a few picosecond THz pulse. This THz pulse is collimated and focused onto the sample with a silicon lens and a pair of off-axis parabolic mirrors (OAPs). The transmitted pulse is then focused with a second pair of OAPs onto a detector antenna. The second part of the NIR pulse arrives at the receiver antenna at the same time as the THz pulse and photoexcites charge carriers in the antenna gap. The electric field of the THz pulse drives the photoexcited charge across the antenna gap, producing a current. The current is converted to a voltage using an SRS 570 transimpedance amplifier and measured by an SRS 830 lockin amplifier. A delay stage is used to vary the arrival time of the THz pulse at the detector antenna and map out the full THz electric field as a function of time. A mechanical chopper is used to modulate the NIR light incident on the emitter at $\sim 800$ Hz. The sample is mounted in a helium-vapor cryostat capable of temperatures ranging from $1.6 - 300$ K.

Once the full time domain THz electric field is collected, it is Fourier transformed to obtain the full complex transmission of the sample. As both the amplitude and phase of the THz electric field are collected, the full complex transmission coefficient can be obtained without use of Kramers-Kronig analysis.

## 2 THz Analysis

As described in the main text, in order to achieve sufficiently high resolution to discern the individual $m1-m9$ excitations, the time domain electric field is collected for 60 ps. However, this long collection time introduces difficulties, as the spectroscopy is being performed on a 600 $\mu$m thick single crystal of $CoNb_2O_6$ with an index of refraction of $\sim 5.4$. With these parameters, reflections of the THz pulse are observed in the time domain spaced by approximately 22 picoseconds. These reflected pulses in

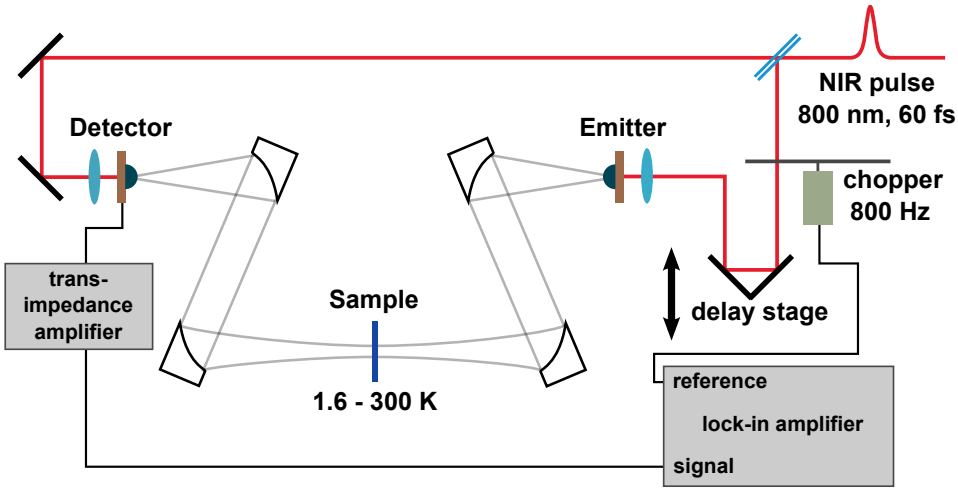


Fig. S1: Time domain terahertz spectroscopy transmission experimental setup.

the time domain manifest themselves as Fabry-Perot oscillations in the frequency spectrum, with an amplitude large enough to obscure the fine magnetic structure. In principle sufficient knowledge of the frequency dependent index of refraction should make it possible to numerically remove these oscillations, however, in practice the required level of precision needed in the index of refraction is too high. Instead, we developed a method of data analysis that exploits the fact that the index of refraction of the material changes fairly slowly with temperature (aside from the absorption due to magnetic excitations), and therefore referencing between scans with similar temperatures will remove the oscillations.

The measured spectral amplitude of the THz pulse is given by:

$$\begin{aligned} S_{measured}(\omega,T,\tau) &= S(\omega,\tau)\cdot t_{magnetic}(\omega,T,\tau) \\ &\quad \cdot t_{background}(\omega,T,\tau)\cdot t_{Fabry-Perot}(\omega,T,\tau) \end{aligned} \tag{1}$$

where $\omega$ is the terahertz frequency, $T$ is the temperature where the measurement is made, and $\tau$ is the time length of the collected scan. This time $\tau$ directly determines the frequency resolution of the spectrum ($\Delta\omega = 2\pi/\tau$). Additionally, we can choose different $\tau$ to eliminate the Fabry-Perot oscillations at the expense of spectral resolution, which we will use later. We denote high resolution scans by the long pulse duration $\tau_L$ and low resolution scans by the shorter THz pulse duration $\tau_S$. $S(\omega,\tau)$ is the spectrum of the initial waveform incident on the $CoNb_2O_6$ crystal, $t_{magnetic}$ is the transmission change due to the magnetic excitations, $t_{background}$ is the change in transmission due to any non-magnetic sources (here mainly cause by reflection at the surface of the crystal and essentially $T$ independent for the temperatures used here), and $t_{Fabry-Perot}$ characterizes the Fabry-Perot oscillations caused by the reflections of the pulse within the crystal.

Our goal is to resolve the magnetic excitations in the system $m1 - m9$ at temperature $T_0$ below

the antiferromagnetic interchain ordering temperature 1.97 K. The first step in the analysis is to divide the high resolution spectrum at $T_0$ by a spectrum at a nearby temperature $T_{R1}$, to remove the Fabry-Perot oscillations.

$$\begin{aligned}\frac{S(\omega,T_0,\tau_L)}{S(\omega,T_{R1},\tau_L)} &= \frac{S(\omega,\tau_L)\cdot t_{magnetic}(\omega,T_0,\tau_L)}{S(\omega,\tau_L)\cdot t_{magnetic}(\omega,T_{R1},\tau_L)} \\ &\cdot\frac{t_{background}(\omega,T_0,\tau_L)\cdot t_{Fabry-Perot}(\omega,T_0,\tau_L)}{t_{background}(\omega,T_{R1},\tau_L)\cdot t_{Fabry-Perot}(\omega,T_{R1},\tau_L)}\end{aligned} \tag{2}$$

As the background reflection is expected to change very slowly with temperature, the two $t_{background}$ terms will cancel. If the magnetic absorption is weak and the change in the index of refraction is small between the temperatures $T_0$ and $T_{R1}$, the two $t_{Fabry-Perot}$ terms cancel as well, leaving us with

$$\frac{S(\omega,T_0,\tau_L)}{S(\omega,T_{R1},\tau_L)} = \frac{t_{magnetic}(\omega,T_0,\tau_L)}{t_{magnetic}(\omega,T_{R1},\tau_L)} \tag{3}$$

This brings us closer to isolating the high resolution magnetic response at $T_0$. However, the magnetic absorption at $T_{R1}$ is still significant, as in our analysis we used $T_{R1} = 3.0$ K to cancel the Fabry-Perot oscillations as fully as possible. In order to isolate the high resolution transmission at the low temperature $T_0$, we need to account for the magnetic absorption signal at the higher temperature $T_{R1}$. We note that as shown in Fig. 2a in the main text, absorption above the ordering temperature is intrinsically broad, and eliminating reflections by only collecting for $\tau_S$ will still allow the absorption at $T_{R1}$ to be fully resolved. To remove $t_{magnetic}$ at $T_{R1}$, we multiply by the ratio of the low resolution ($\tau_S$) spectra at $T_{R1}$ and a new higher reference temperature ($T_{R2}$) that is well above the onset of ferromagnetic correlations that begin near 25 K. The low resolution scans of length $\tau_S$ avoid Fabry-Perot oscillations in the spectra. Here we use $T_{R2} = 60$ K.

$$\begin{aligned}\frac{S(\omega,T_0,\tau_L)}{S(\omega,T_{R1},\tau_L)}\cdot\frac{S(\omega,T_{R1},\tau_S)}{S(\omega,T_{R2},\tau_S)} &= \frac{t_{magnetic}(\omega,T_0,\tau_L)}{t_{magnetic}(\omega,T_{R1},\tau_L)}\cdot\frac{S(\omega,\tau_S)\cdot t_{magnetic}(\omega,T_{R1},\tau_S)}{S(\omega,\tau_S)\cdot t_{magnetic}(\omega,T_{R2},\tau_S)} \\ &\cdot\frac{t_{background}(\omega,T_{R1},\tau_S)\cdot t_{Fabry-Perot}(\omega,T_{R1},\tau_S)}{t_{background}(\omega,T_{R2},\tau_S)\cdot t_{Fabry-Perot}(\omega,T_{R2},\tau_S)}\end{aligned} \tag{4}$$

We assume again the the background absorption at $T_{R1}$ and $T_{R2}$ are identical, and thus cancel. For these short time scans, $t_{Fabry-Perot} = 1$, which leaves

$$\frac{S(\omega,T_0,\tau_L)}{S(\omega,T_{R1},\tau_L)}\cdot\frac{S(\omega,T_{R1},\tau_S)}{S(\omega,T_{R2},\tau_S)} = \frac{t_{magnetic}(\omega,T_0,\tau_L)}{t_{magnetic}(\omega,T_{R1},\tau_L)}\cdot\frac{t_{magnetic}(\omega,T_{R1},\tau_S)}{t_{magnetic}(\omega,T_{R2},\tau_S)} \tag{5}$$

We specifically chose $T_{R2}$ to be above the ferromagnetic ordering temperature, so that the magnetic transmission component $t_{magnetic}(\omega,T_{R2},\tau_S) = 1$ and we are left with

$$\frac{S(\omega,T_0,\tau_L)}{S(\omega,T_{R1},\tau_L)}\cdot\frac{S(\omega,T_{R1},\tau_S)}{S(\omega,T_{R2},\tau_S)} = t_{magnetic}(\omega,T_0,\tau_L)\cdot\frac{t_{magnetic}(\omega,T_{R1},\tau_S)}{t_{magnetic}(\omega,T_{R1},\tau_L)} \tag{6}$$

As described earlier, above the ordering temperature the magnetic absorption becomes broad, such that the high and low resolution scans should have the same linewidth, and thus their ratio

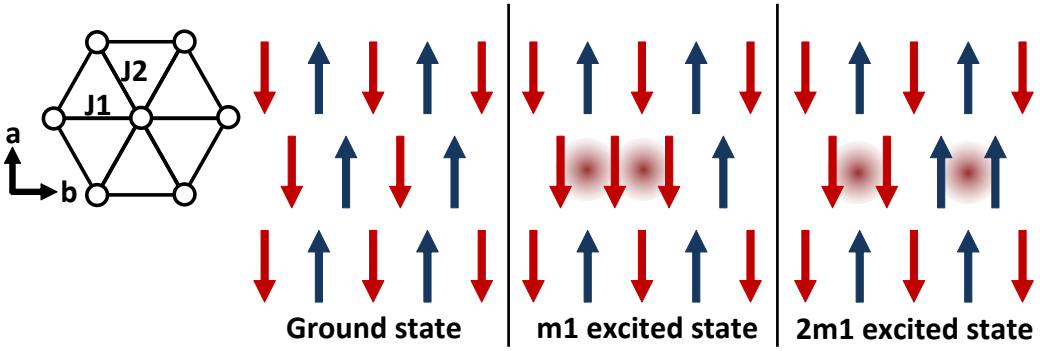


Fig. S2: Diagram of the $m1$ and $2m1$ excitations in the low temperature ordered state. The exchange interaction along the $b$-direction has a strength $J_1$, while along the diagonals in the ab-plane the interaction strength is $J_2$. Both the $m1$ and $2m1$ break two $J_1$ exchange interactions while leaving the total energy due to $J_2$ exchange unchanged.

should be 1, leaving us with just the transmission due to the high resolution scan in the ordered state at $T_0$.

$$\frac{S\left(\omega, T_0, \tau_L\right)}{S\left(\omega, T_{R1}, \tau_L\right)} \cdot \frac{S\left(\omega, T_{R1}, \tau_S\right)}{S\left(\omega, T_{R2}, \tau_S\right)} = t_{magnetic}\left(\omega, T_0, \tau_L\right) \tag{7}$$

We have confirmed that the final high resolution magnetic absorption spectra do not depend on the precise temperatures chosen or the exact time intervals chosen for $\tau_L$ and $\tau_S$.

## 3 Energy of the $2m1$ excitation

The energy of a bound state excitation on a single chain ($m1-m9$) can be calculated in the confined kink model using Eq. 2 in the main text. There, $2m_0$ is the energy cost of the ferromagnetic intrachain exchange interaction at the two domain walls. The second term, $E_{mf} = z_1\lambda^{2/3}\left(\frac{\hbar^2}{\mu}\right)^{1/3}$, is the energy cost to break the mean field interaction caused by the interchain ordering.

To create two $m1$ excitations, 4 domain walls must be created at an energy cost of $4m_0$. If the excitations occur on the same chain, each $m1$ excitation pays the cost of the mean field interaction, for a total excitation energy of $4m_0 + 2E_{mf}$, double the energy of a single $m1$ excitation. As Fig. 3a in the main text shows, the observed energy is lower than this. However, if two $m1$ excitations are created on sites on adjacent chains in the ab-plane, the mean field energy cost is reduced from $2E_{mf}$ to $E_{mf}$, so that the total energy will be

$$E_{2m1} = 4m_0 + z_1\lambda^{2/3}\left(\frac{\hbar^2}{\mu}\right)^{1/3} \tag{8}$$

which is much closer to the observed $2m1$ energy. We use the values for the constants from Coldea et al., with $m_0 = 0.5035$ meV and $\lambda^{2/3}\left(\hbar^2/\mu\right)^{1/3} = 0.0798$ meV. The mechanism of this excitation is depicted in Fig. S2. The chains are shown below the ordering temperature of 1.97 K.

Each arrow represents a ferromagnetically aligned chain coming out of the page in the c-direction. The chains order antiferromagnetically along the b-direction. The exchange interactions along the b-direction have a strength $J_1$, while along each diagonal the exchange interaction strength is $J_2$, with both interactions being antiferromagnetic.

When a single spin flip occurs, there is no change in the total energy due to exchange along the diagonals, $J_2$. However, the exchange interaction $J_1$ is broken between the two neighboring spins in the b-direction, which costs total energy $E_{mf}$.

When two spin flips occur simultaneously on neighboring spin chains, the $2m1$ excited state is formed. Again, the total energy of the exchange interaction due to $J_2$ remains the same, and two $J_1$ interactions are broken, again at a total cost $E_{mf}$, making the total energy of the excited state $4m_0 + E_{mf}$.

# 4 Sample preparation

Stoichiometric amounts of $Co_3O_4$ and $Nb_2O_5$ were thoroughly ground together by placing them in an automatic grinder for 20 minutes. Pellets of the material were pressed and heated at 950° C with one intermittent grinding. The powder was then packed, sealed into a rubber tube evacuated using a vacuum pump, and formed into rods (typically 6 mm in diameter and 70 mm long) using a hydraulic press under an isostatic pressure of 7x$10^7$ Pa. After removal from the rubber tube, the rods were sintered in a box furnace at 1375° C for 8 hours in air.

Single crystals approximately 5 mm in diameter and 30 mm in length were grown in a four-mirror optical floating zone furnace at Johns Hopkins (Crystal System Inc. FZ-T-4000-H-VII-VPO-PC) equipped with four 1-kW halogen lamps as the heating source. Growths were carried out under 2 bar $O_2$-Ar (50/50) atmosphere with a flow rate of 50 mL/min, and a zoning rate of 2.5 mm/h, with rotation rates of 20 rpm for the growing crystal and 10 rpm for the feed rod. Measurements were carried out on oriented samples cut directly from the crystals using a diamond wheel.

Cut samples were polished to a finish of 3 $\mu$m and total thickness of $\sim$ 600 $\mu$m using diamond polishing paper and a specialized sample holder to ensure that plane parallel faces were achieved for the THz measurement. The discs were approximately 5 mm in diameter. Three different orientations were cut, each with a different crystallographic axis oriented normal to the sample face.

# 5 The four-kink bound state

The observation of the new $2m1$ bound state of $m1$ excitations on adjacent chains is one of the major results of the work. To further understand the nature of this excitation, we carried out calculations of its energy and dispersion. We start with a system of four kinks, two each on two adjacent Ising chains. It is clear from Fig. S2 that only the exchange interaction $J_1$ contributes to kink confinement and the corresponding effective longitudinal field is $h_z = 4J_1$. Hence, while studying kink bound states, we can safely ignore the couplings between the different chains in the $a$-direction and work in just two dimensions (the $c-b$ plane). The four-kink potential then depends on which $J_1$ bonds are frustrated in a given configuration. One can read off this potential directly

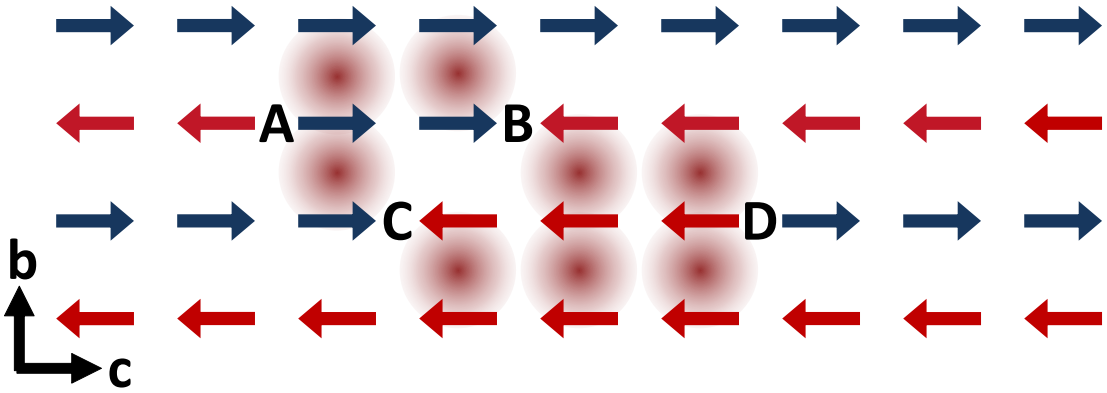


Fig. S3: A typical four-kink configuration. The four kinks where intrachain order is broken at an energy cost of $J/2$ each are labeled as A, B, C and D. Sites where interchain ordering is broken are shown by colored red clouds.

from Fig. S3, which takes the form

$$\begin{aligned} V(x_A, x_B, x_C, x_D) &= 4J_1[(x_D - x_C) + (x_B - x_A)] \ \ if \ \ x_D < x_A \ \ or \ \ x_B < x_C \\ &= 2J_1[|x_A - x_C| + |x_B - x_D|] + 2J_1[(x_D - x_C) + (x_B - x_A)] \ \ otherwise \end{aligned}$$

In addition, there is the hard-wall constraint $x_B > x_A$ and $x_D > x_C$ between the kinks on any one Ising chain. Thus the effective Hamiltonian for this four-kink system consists of two copies of the two-kink Hamiltonian which appears in the supplementary material to Coldea et. al. [5] with $V$ replacing the simple linear two-kink attractive potential. It is interesting to note that the two spin-clusters (on the two adjacent $b$-chains) attract each other only when there is an overlap between them. Otherwise, they are essentially free. We found out that this inter-cluster potential, despite having a strictly finite range, accomodates at least one bound state.

To see this, we first write the four-kink Hamiltonian in a basis labelled by the centres-of-mass (COMs) of the two clusters $i$ and $j$ and their lengths $m > 0$ and $n > 0$.

$$\begin{aligned} H|i,m;j,n> = (2J + V(i,j,m,n))|i,m;j,n> - \alpha[|i+\frac{1}{2},m+1;j,n> + |i+\frac{1}{2},m-1;j,n> \\ + |i-\frac{1}{2},m+1;j,n> + |i-\frac{1}{2},m-1;j,n> + |i,m;j+\frac{1}{2},n+1> + |i,m;j+\frac{1}{2},n-1> \\ + |i,m;j-\frac{1}{2},n+1> + |i,m;j-\frac{1}{2},n-1>] - \beta_0\delta_{m,1}[|i-1,m;j,n> + |i+1,m;j,n>] \\ - \beta_0\delta_{n,1}[|i,m;j-1,n> + |i,m;j+1,n>] + \beta_1\delta_{m,1}|i,m;j,n> + \beta_1\delta_{n,1}|i,m;j,n> \end{aligned}$$

Here $J$ is the energy cost to create a pair of kinks on one Ising chain, $\alpha$ is the effective transverse field causing the kinks to hop, $\beta_0$ is the kinetic energy gain for two nearest neighbor kinks hopping together and $\beta_1$ is the extra energy cost of two adjacent kinks (i.e. a single spin flip) [5]. One can now transform to a more natural set of coordinates: the COM of the whole system $u = (i+j)/2$ and the relative separation of the two clusters $v = (i-j)$. The Hamiltonian has a discrete translational symmetry with respect to $u$ and hence can be partially diagonalized by Fourer transforming from

the basis $\{|u, v; m, n>\}$ to the basis $\{|k, v; m, n>\}$. The problem now becomes a 3D lattice model, $v, m, n$ being the lattice coordinates, for every wavevector $k$ within the first Brillouin zone $[-\pi, \pi]$.

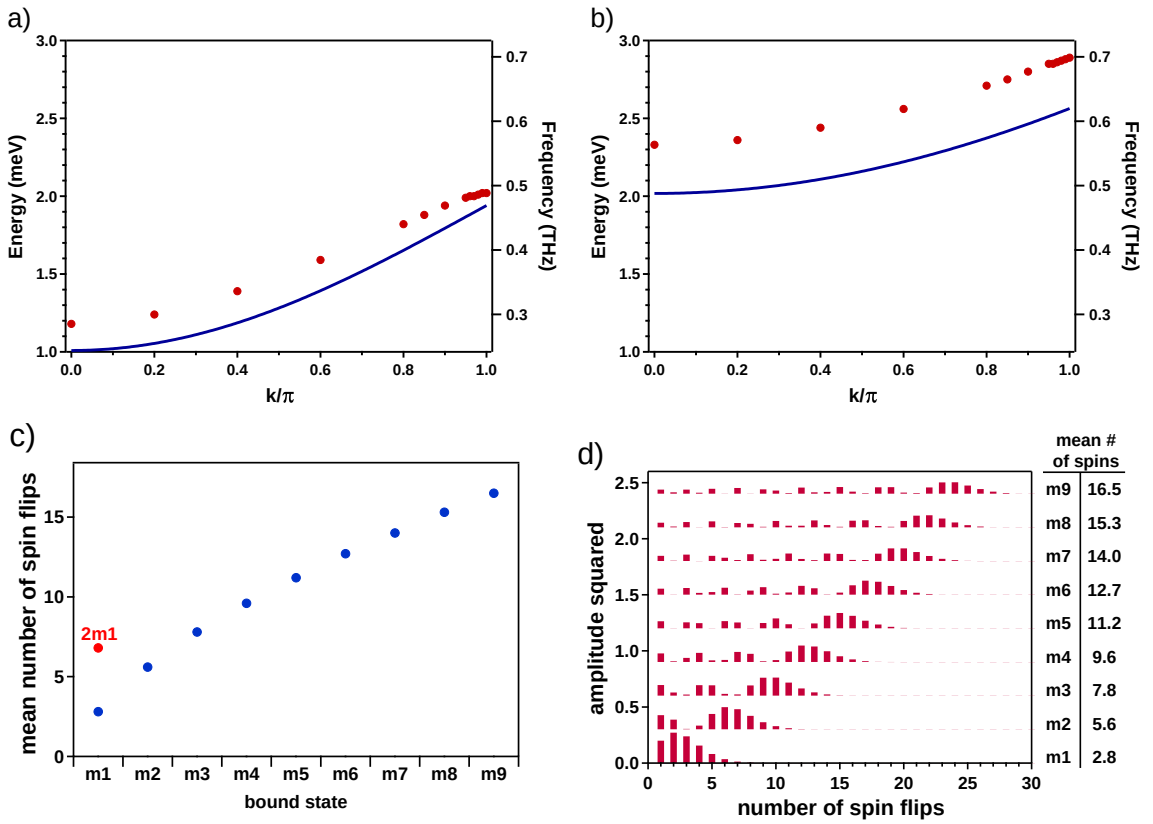


Fig.S4: Dispersion of the ground state of the (a) two-kink system (b) four-kink system (red points). The dispersions are flat near the zone center and sharp near the edge, which match the features of the bottoms of the corresponding continua at zero longitudinal field (blue lines). (c) The weighted mean number of spin flips in the m1 - m9 and 2m1 states. (d) Squared amplitudes for the wavefunctions for m1 - m9 states in the spin flip basis. Numerical values of the weighted mean number of spin flips shown in (c) are listed in the table.

The spectrum of the four-kink system definitely has a continuum because two non overlapping spin-clusters are essentially free. We tried to investigate if the spectrum has bound states in addition to this continuum. To do this, we first studied a two-kink system on one Ising chain which can easily be solved numerically. The two kinks in the ground state of this system are well localized within $L \sim 10$ lattice units from each other. This implies that if there are four-kink bound states, the values of $m$ and $n$ in the lowest-lying state will be localized approximately within the same distance $L$. In that case, the range of the inter-cluster potential is $v \in [-L, L]$ and outside this range the four-kink wave-function should fall off exponentially.

Thus, if there is a bound state, the wave function will be localized within $[-aL, aL]$ in the $v$-direction for some $a$. Because the $v$ coordinate can assume half integer values, this means that we now need to find the lowest eigenvalue and the corresponding eigenstate of our reduced model within an $L \times L \times 4aL$ lattice with hard wall boundary conditions at the six faces. We can then vary $L$ and $a$ to check convergence of the energy. For $L = 10$ and $a = 2$ this reduces to the diagonalization problem of a $8000 \times 8000$ sparse matrix which can be easily done numerically.

As a starting point, we took $a = 2$. At $k = 0$ the ground state energy converges to $2.33\,\mathrm{meV} = 564\,\mathrm{GHz}$ for $L = 8$ and stays constant (up to the second decimal place) for $L = 8, 9, 10, 11$. Increasing $a$ to 3 does not change the energy either (up to the fifth decimal place). This indicates that we are actually seeing a stable bound state because $E_{bound}(k = 0)$ is less than the bottom of the two-cluster continuum at 572 GHz that we find from our calculations.

The calculation was repeated for finite wavevectors and the dispersion of this bound state $E(k)$ in the first Brillouin zone was obtained. A plot of this dispersion is shown in Fig. S4. (Due to symmetry of the Hamiltonian, $E(k) = E(-k)$.) A plot of the two-kink ground state dispersion is also shown for comparison. It can be seen that the four-kink state is less dispersive than the two-kink state. This is expected because in the absence of any interaction between kinks, the spectrum forms a continuum. If a weak interaction is then turned on, the ground state dispersion is expected to track the bottom envelope of this continuum. It is easily seen that the bottom of the four kink coninuum is indeed flatter than the two kink one. In addition, these continua are flat at $k = 0$ and have sharp edges at $k = \pi$. These features can also be seen in the bound state dispersions.

If we strictly confine ourselves to the four-kink Hilbert space, the spectral weight of the above bound state (which depends on its overlap with the single spin flip state) vanishes. But in the real material a kink pair can be created/annihilated on an Ising chain by the transverse field term in the Hamiltonian. This tunnelling mechanism between the the above state and the two-kink eigenstates endows it with a finite spectral weight which can be calculated in first-order perturbation theory. The spectral weight thus obtained for the $2m1$ excitation is 0.17 which lies roughly halfway between the (theoretical) $m1$ and $m2$ spectral weights (0.20 and 0.13 respectively). This theoretical spectral weight is greater than what is observed experimentally from the absorption (taking into account the relative weighting of $\chi(\omega)$ by $\omega$). However, it qualitatively supports the interpretation of the $2m1$ peak as a separate excitation from the $m1$-$m9$ series, not a tenth $m10$ bound state. The theoretically predicted spectral weights for the $m1$, $m2$, etc. excitations decrease monotonically, with the $m9$ and $m10$ spectral weights being only 0.037 and 0.033, respectively. The significantly increased spectral weight of the $2m1$ excitation compared to the $m9$ excitation therefore supports the interpretation of the $2m1$ excitation as a bound state of $m1$ bound states on adjacent chains.